Chapter 9

Hydrodynamic Simulations of the Decay Phase: Testing Suppression of Conduction

9.1 Introduction

Suppression of thermal conduction by turbulence plays important roles in many astrophysical and space plasma environments. Chandran & Cowley (1998), for example, found entangled magnetic fields in a turbulent intracluster plasma can reduce the Spitzer (1962) conductivity by a factor of 10^2–10^3.

For solar flares, Jiang et al. (2006) reported spatial confinement and lower than expected energy decay rate of the X-ray loop-top (LT) source during the flare decay phase observed by *RHESSI* . This observation was interpreted as suppressed thermal conduction and/or simultaneous heating, which were assumed to be produced by turbulence or plasma waves at the LT. The same turbulence, with different strength and other properties, could also be responsible for acceleration of particles during the impulsive phase.

Jiang et al. (2006) assumed that the plasma in the flaring loop is in a hydrostatic state, which works well as a zeroth order approximation and made their semi-analytical work tractable. Antiochos & Sturrock (1978), however, from their simplified analytical derivation, found the bulk flow of the plasma could suppress thermal conduction as well, but they did not include radiative loss in their model. Plasma flows (or convection), in general, can carry energy from one place to another, in a way that works in parallel with thermal conduction.

It is thus necessary to improve on previous works by Jiang et al. (2006) and Antiochos & Sturrock (1978) by including the hydrodynamic response of the plasma, its feedback to the conduction, and a full calculation of radiative loss. This will help shed light on energy transport and the evolution of the flaring plasma. We will also extend the domain considered in Jiang et al. (2006) to beneath the transition region, such that we can include all the energy flow channels, i.e., radiative loss in the chromosphere and possible conduction flux through there. Such a work is reported in this chapter. The numerical model and simulation result are presented in §9.2 and §9.3, respectively. We summarize the main findings in §9.4.

9.2 Simulation Model of Suppression of Conduction and Plasma Heating

We use the NRL flux-tube model by Mariska et al. (1989), as described in Chapter 7. The only difference here is that we used the abundance in the original code, i.e., helium being 6.3% of the hydrogen number density, rather than a simply pure hydrogen plasma. Accordingly, the mean ionic charge is taken as $Z = 1.059$ and the mean mass per particle is $\mu = 0.5724$ in units of proton masses m_p. We have adopted the suppression of conduction and additional heating due to turbulence from Jiang et al. (2006), with necessary modifications due to the absence of the isobaric condition, which we describe as follows.

The electron, ion (as in Chapter 7), and combined Spitzer conductivities are

$$\kappa_e = 1.1 \times 10^{-6} T_e^{5/2}, \qquad \kappa_i = \kappa_e/25, \tag{9.1}$$

$$\kappa = \kappa_e + \kappa_i = \kappa_S T^{5/2} \text{ (where } \kappa_S = 1.14 \times 10^{-6} \text{ ergs cm}^{-1}\,\text{s}^{-1}\,\text{K}^{-7/2}), \tag{9.2}$$

in which we assume $T_e = T_i = T$. The corresponding conductive heat flux is

$$\mathcal{F}_{\text{Spit}} = \kappa \nabla T = \kappa_S T^{5/2} \nabla T \,. \tag{9.3}$$

Following Jiang et al. (2006), in presence of suppression of thermal conduction, the conductive flux should be modified as (Spicer, 1979):

$$\mathcal{F}_{\text{cond}} = \frac{1}{1 + \tau_{\text{sc}}^{-1}/\tau_{\text{Coul}}^{-1}} \mathcal{F}_{\text{Spit}} = \left(\frac{\kappa_S T^{5/2}}{1 + \tau_{\text{sc}}^{-1}/\tau_{\text{Coul}}^{-1}} \right) \nabla T \,, \tag{9.4}$$

where

$$\tau_{\text{Coul}}^{-1} \simeq 150 \left(\frac{T}{10^7\,\text{K}} \right)^{-3/2} \left(\frac{n_e}{10^{11}\,\text{cm}^{-3}} \right) \quad \text{s}^{-1} \tag{9.5}$$

is the mean Coulomb collision rate of the thermal electrons carrying the heat flux, and the mean wave scattering rate is assumed to be a Gaussian (width w) function of distance ($l = s_{\text{max}} - s$) from the loop apex,

$$\tau_{\text{sc}}^{-1} = 150 \mathcal{S}_0 \exp[-(l/w)^2] \quad \text{s}^{-1} \,, \tag{9.6}$$

such that the ratio of the wave scattering to Coulomb collision rate is

$$\tau_{\text{sc}}^{-1}/\tau_{\text{Coul}}^{-1} = S(s) \left(\frac{T}{10^7\,\text{K}} \right)^{3/2} \left(\frac{n}{10^{11}\,\text{cm}^{-3}} \right)^{-1} \,, \tag{9.7}$$

where $\mathcal{S}(l) = \mathcal{S}_0 \exp[-(l/w)^2]$ and the dimensionless $\mathcal{S}_0$ represents the strength of suppression (and of turbulence). Note that here we dropped the isobaric assumption taken by Jiang et al. (2006), which is not necessarily satisfied in a dynamic flare loop. Consequently equation (9.7) here is slightly different from that given by Jiang et al.

For a given turbulence condition, the inverse of the corresponding particle acceleration

(or heating) timescale is (Jiang et al., 2006)

$$\tau_{\text{ac}}^{-1} \simeq \xi(v_{\text{A}}/v_{\text{th}})^2 \tau_{\text{sc}}^{-1} = \xi \left(\frac{B^2 m_e}{12\pi k_B \rho T} \right) \tau_{\text{sc}}^{-1} \,, \tag{9.8}$$

where $v_{\text{A}} = B/(4\pi\rho)^{1/2}$ is the Alfvén velocity (B the magnetic field), $v_{\text{th}} = (3k_{\text{B}}T/m_e)^{1/2}$ is the thermal velocity of the electrons (m_e the electron mass), and the coefficient ξ depends on the wave spectrum and wave-particle coupling (Schlickeiser, 1989). Accordingly, the energy change (heating) rate can be written as

$$\dot{\mathcal{E}}_h \;=\; U_{\text{th}}\tau_{\text{ac}}^{-1} = U_{\text{th}}\xi \left(\frac{B^2 m_e}{12\pi k_B \rho T} \right) \tau_{\text{sc}}^{-1} \tag{9.9}$$

$$\;=\; \frac{25}{2\pi} \left(\frac{m_e}{\mu m_p} \right) \frac{\mathcal{S}_I}{\gamma - 1} \exp[-(l/w)^2](\xi B^2)\,, \tag{9.10}$$

where we have substituted equations (9.6) and (9.8), and used $U_{\text{th}} = P/(\gamma - 1)$ for the thermal energy density, and $P = P_e + P_i = (n_e + n_i)k_BT = \rho k_BT/\mu m_p$ for the pressure. We use this $\dot{\mathcal{E}}_h$ for the heating rate S_e in equation (7.37) in the HD calculation and use ξB^2 as a parameter to adjust the relative importance of heating (vs. suppression of conduction, see discussions in §3 of Jiang et al., 2006).

9.3   Numerical Results

We have performed a simulation of four cases with model parameters summarized in Table 9.1. For each case, we used the data saved at $t = 64\,\text{s}$ from a previous impulsive phase simulation as the initial state, from which we continue the calculation. A uniform background heating of $8.31 \times 10^{-3}\,\text{ergs}\,\text{s}^{-1}\,\text{cm}^{-3}$ (same as that used in Chapter 7, which translates to a total energy input rate of $2.35 \times 10^{22}\,\text{ergs}\,\text{s}^{-1}$)[1] was applied. On top of that, for Cases B and C, we alternatively applied additional heating ($\dot{\mathcal{E}}_h$, or S_e) and suppression of conduction, respectively; for Case D, we used both additional heating and suppression, while we used none of them for Case A.

Table 9.1: Summary of simulation cases.

Cases	model	ξB^2	$\mathcal{S}_0$	mean energy decay ($10^{24}\,\text{ergs}\,\text{s}^{-1}$)	n_e ($10^{10}\,\text{cm}^{-3}$)	T ($10^6\,\text{K}$)
A	none	–	–	8.07	6.16	1.48
B	heating only	10	20	6.66	7.78	6.54
C	suppression	0	20	7.24	4.68	7.20
D	heating & suppression	10	20	6.01	4.11	15.9

Note — The mean energy decay rate is calculated for the time interval of $[0, 500\,\text{s}]$. n_e and T are the values at the loop apex at $t = 500$ s.

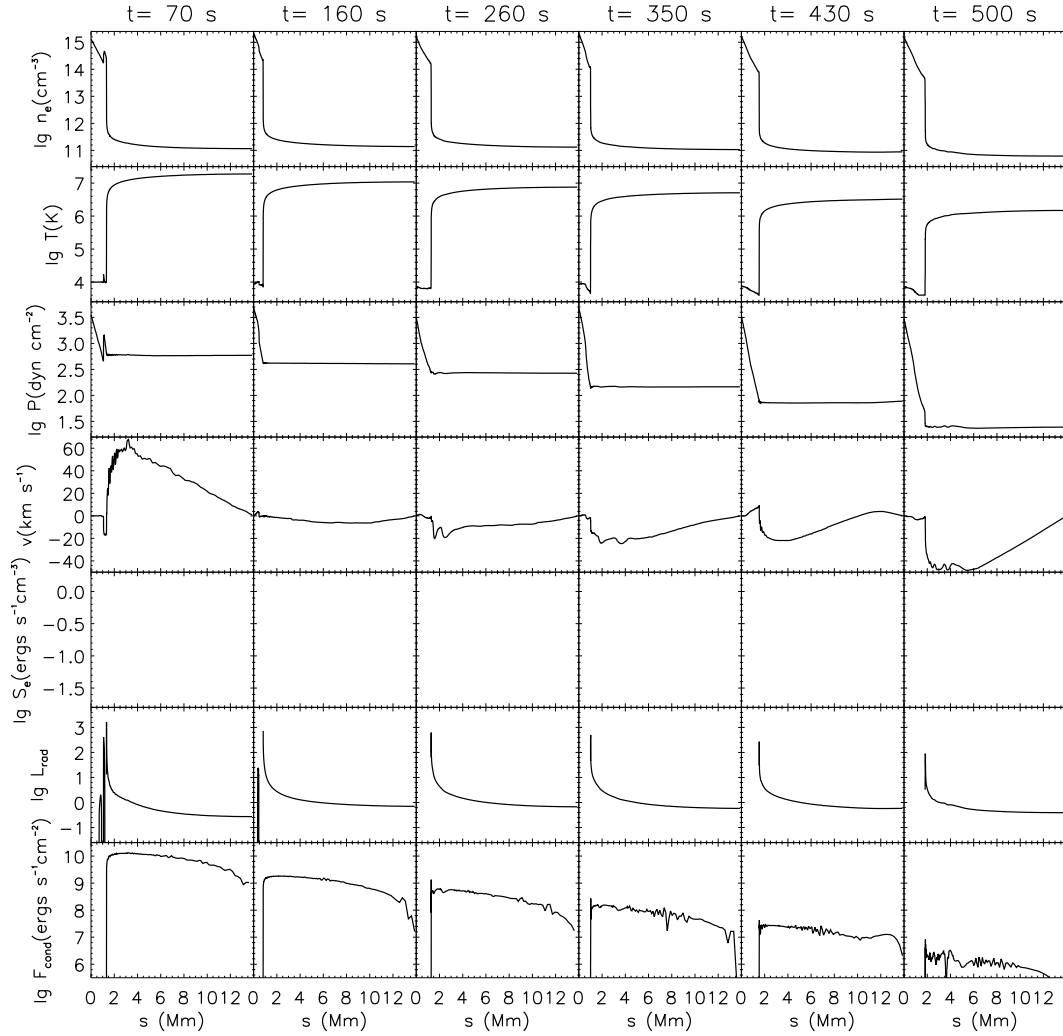[1] As we will see later, this amount of energy input is negligible compared with the other energy contents.

Figure 9.1: HD evolution of various quantities for Case A: electron number density, temperature, gas pressure, upward velocity, heating rate S_e, radiative loss rate L_{rad} (in same units as S_e), and heat conduction flux F_{cond}, as a function of distance from the bottom (FP) of the loop. Note that $S_e = 0$ in this Case and the corresponding panels are left blank intentionally for a better comparison with the other cases.

9.3.1   Case A: No Heating or Suppression of Conduction

Figure 9.1 shows the evolution of various HD variable as a function of distance along the loop (from the bottom, cf., Fig. 7.3). The system starts with a hot, relatively dense corona, heated by electrons during the preceding impulsive phase. We find the density and temperature in the coronal portion of the loop decreases with time. This occurs because of cooling in the form that heat conduction (*bottom*, not suppressed here) carries energy to the transition region and the upper chromosphere where radiative loss function (second to the *bottom*) peaks, and then energy is radiated away there. Note that direct radiative loss in the upper corona is negligibly small compared with conductive cooling (also see, e.g., Jiang et al., 2006). As a result of cooling and reduced pressure gradient (not sufficient to support material against gravity) in the corona, the plasma simply condenses and falls back to the chromosphere. This can be seen from the velocity curve, which shows generally increasing negative (downward) values. We also note that early in the decay phase (e.g., $t = 70\,$s), however, chromospheric evaporation (upflow) still takes place because of residual conductive heating from the hot corona.
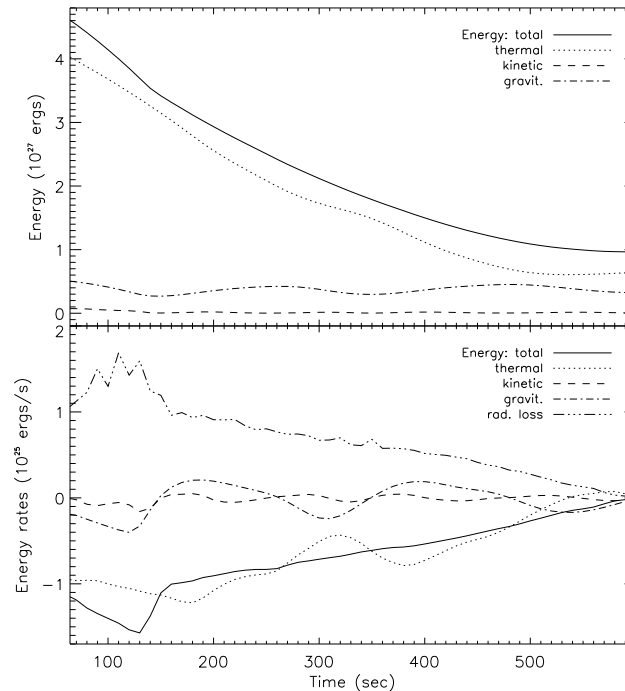

Figure 9.2: Energy evolution for Case A. *top*: Total, thermal, kinetic, and gravitational energy, integrated over the volume of the loop, as a function of time. *bottom*: Time derivative of the above energy contents, together with the radiative loss rate.

The evolution of the energy contents, which are spatially integrated over the loop volume, is shown in Figure 9.2 (*top*). The total energy monotonically decreases with time. The thermal energy (*dotted*) follows the same trend and clearly dominates over the gravitational (*dot-dashed*) and kinetic (*dashed*) energy, which stay at about the same level. The *bottom*

panel shows the time derivatives of these energy contents, together with the radiative loss
rate. We find the absolute value of the total energy change rate decreases with time, which
is correlated with the radiative loss (this simply means energy conservation, see §8.2.1).

We note that there are some fluctuations in the gravitational and kinetic (smaller *ab-
solute* amplitudes) energy, which are more pronounced in the *bottom* panel of Figure 9.2.
The absolute value of the thermal energy change rate (< 0) also show, on top of its gen-
eral decreasing trend, some modulations that seem to be anti-correlated with those of the
gravitational and kinetic energy. We interpret this as conversion of energy among different
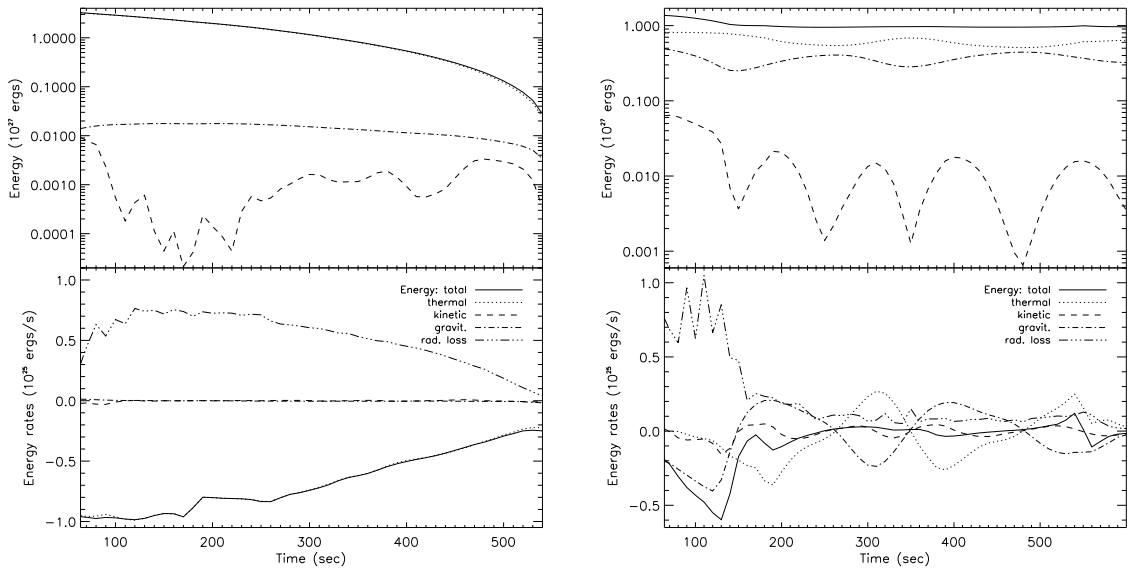forms in the plasma (also see Chapter 8).

Figure 9.3: Same as Fig. 9.2, but for the corona (*left*) and chromosphere (*right*) only.

To see this point clearly and identify the source of the fluctuations, we plot the same
energy budget history for the corona (*left*) and for the chromosphere (*right*) separately in
Figure 9.3 in which we used the position where $T = 1 \times 10^7$ K as the boundary between
the two regions. For the corona portion (Fig. 9.3), the thermal energy and the total energy
curves almost overlap each other, and they simply show a featureless monotonic decay;
so does the gravitational energy. Only the kinetic energy exhibits some fluctuations, but
without a simple pattern. For the chromosphere (Fig. 9.3, *right*, note logarithmic scale),
in contrast, the total energy initially decrease slightly and then stays almost constant and
the fraction of the thermal energy is smaller than that in the corona. The fluctuations
and the anti-correlation of the gravitational and thermal energy are evident. This results
from the **chromospheric oscillation** (Mariska et al., 1982), which can be seen from the
top panel of Figure 9.1, where the height of the transition region rises and drops back and
forth. (This can be more clearly seen in a movie, not shown). The alternative rarefaction
and compression of the chromospheric material performs energy conversion between the two
forms: thermal and gravitational energy. We note that the kinetic energy (Fig. 9.3, *upper
right*) shows larger *relative* amplitudes and, particularly, a ~ 2 times higher frequency than

the gravitational energy. The kinetic energy reaches its minimum when the gravitational energy reaches its maximum or minimum. This is because the chromosphere oscillates like a loaded[2] spring in the vertical direction and each cycle in the gravitational energy variation includes *two* cycles of acceleration and deceleration, resulting two cycles in the kinetic energy curve.
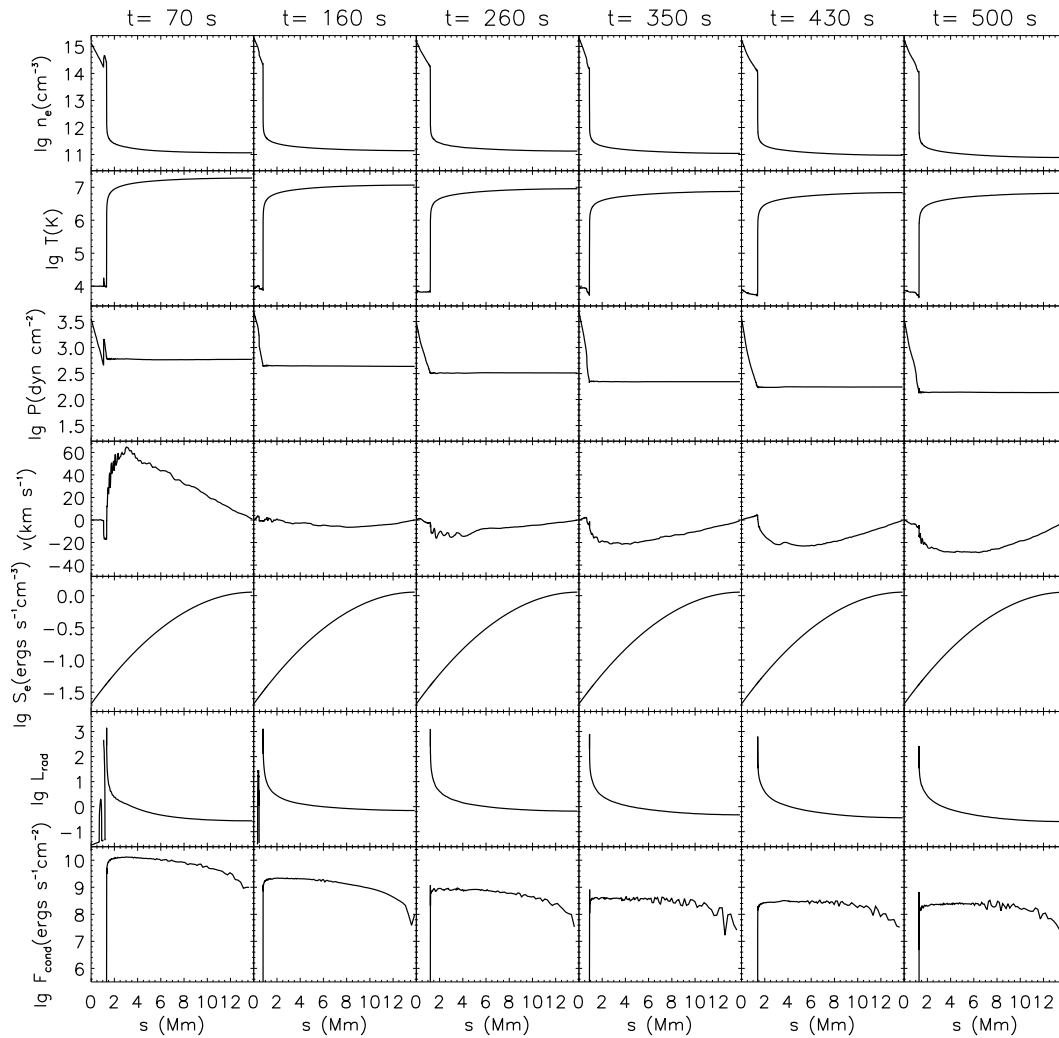
9.3.2　Case B: Heating Only

Figure 9.4: Same as Fig. 9.1, but for Case B.

In this Case, we applied additional heating in the corona. The spatial distribution of

---

[2]Most of the loading is provided by cooling and condensation in the overlying layers in this simulation (Mariska et al., 1982), simply because material falls back from the corona and thus pushes chromosphere downward.

the heating is of a Gaussian shape which peaks at the loop apex (see Fig. 9.4, row 5). The evolution of the HD variable is shown in Figure 9.4, which is very similar to Figure 9.1 for Case A, except that here the coronal density, temperature, and pressure decay slightly more slowly due to heating. Note that the temperature still distributes more or less uniformly in the corona despite more heating at the LT. The downflow (due to condensation) velocity is lower than that in Case A too. The conduction flux stays higher because of higher temperature here. The history of the energy budget (not shown) is also very similar to that of Case A (Fig. 9.2).

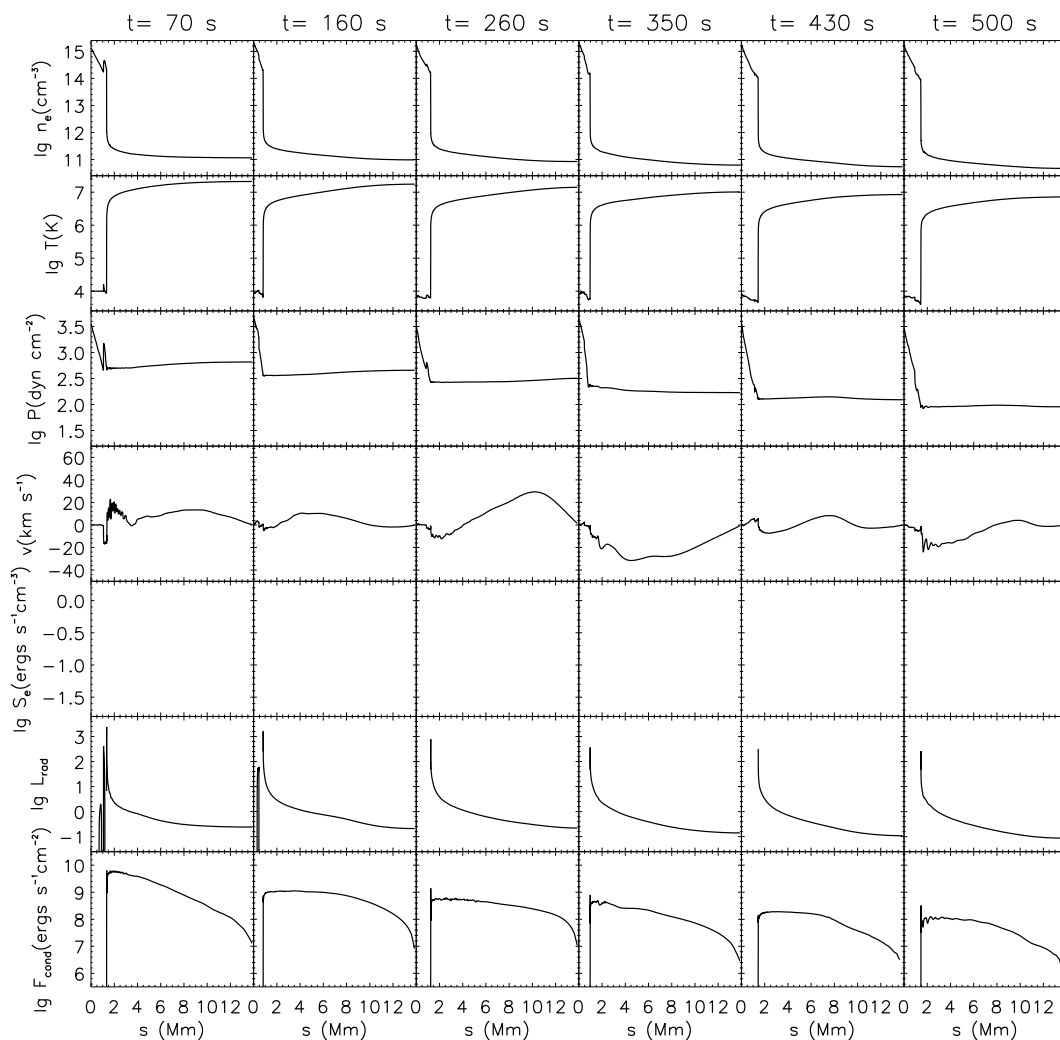### 9.3.3   Case C: Suppression of Conduction Only

Figure 9.5: Same as Fig. 9.1, but for Case C.

Here instead of applying additional heating, we suppress the conduction with a Gaussian

profile. Compared with Case A, the heat conduction flux (Fig. 9.5) varies more dramatically from the LT to the FP. At $t = 70$ s, for example, F_{cond} increases by nearly three orders of magnitude from the loop apex to near the transition region, as opposed to the variation of about one order of magnitude in Case A. As a result, the temperature slope in the corona is larger here (because there is more suppression in the LT than near the FP). The overall temperature decay, as expected, is delayed, compared with Case A. The energy budget is very similar to that of Case D (see below, Fig. 9.7) and thus is not shown here. A new feature caused by suppression of conduction here is the traveling waves (see the velocity in Fig. 9.5) in the corona, for which we defer our discussion to next section.

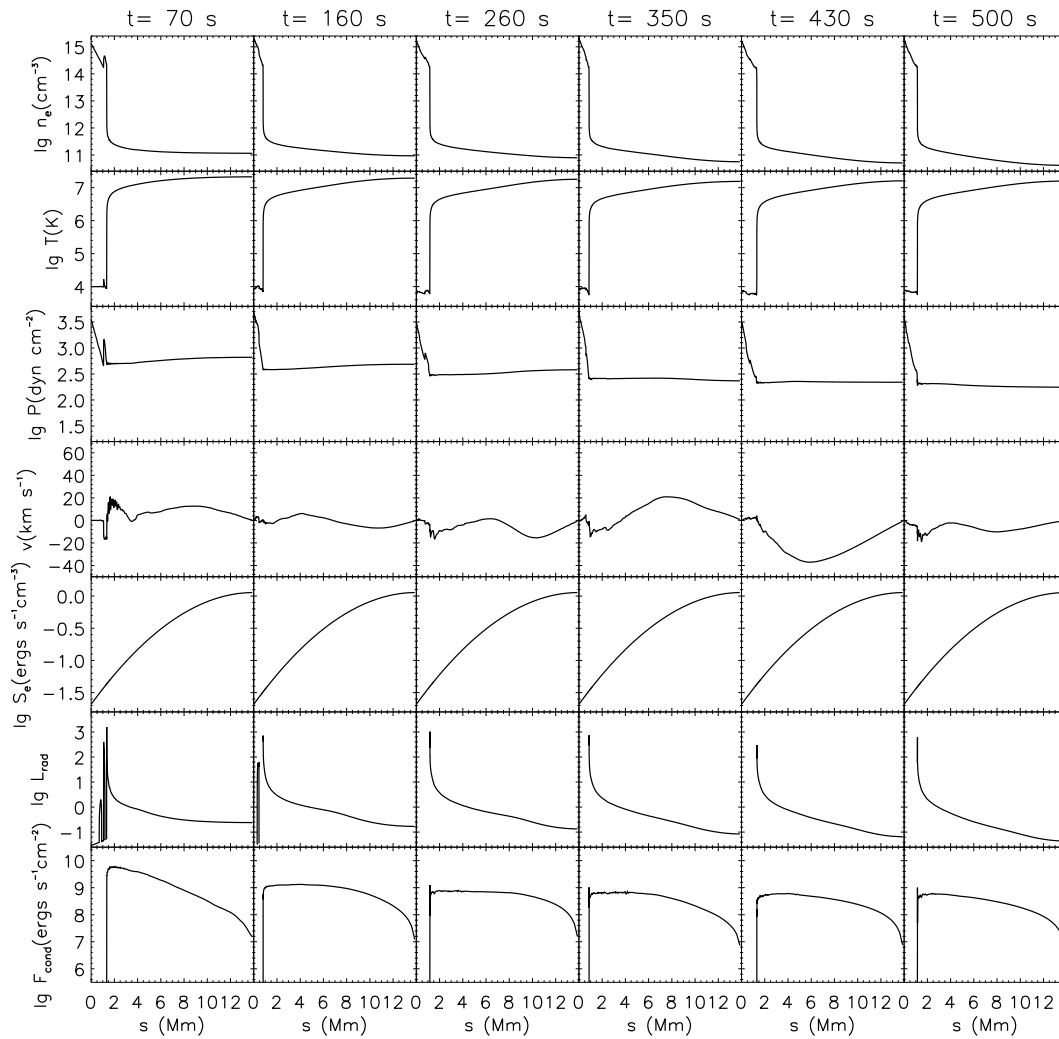### 9.3.4   Case D: Heating and Suppression of Conduction

Figure 9.6: Same as Fig. 9.1, but for Case D.

Now we combine heating and suppression of conduction used above together in Case D. As can be seen in Figure 9.6, the overall evolution is similar to that of Case C, except even more delayed decay here. The energy history is plotted in Figure 9.7 (*left*). The constant heating rate is shown as the *long dashed* line, which in addition to the suppression of conduction, counteracts the energy decay.
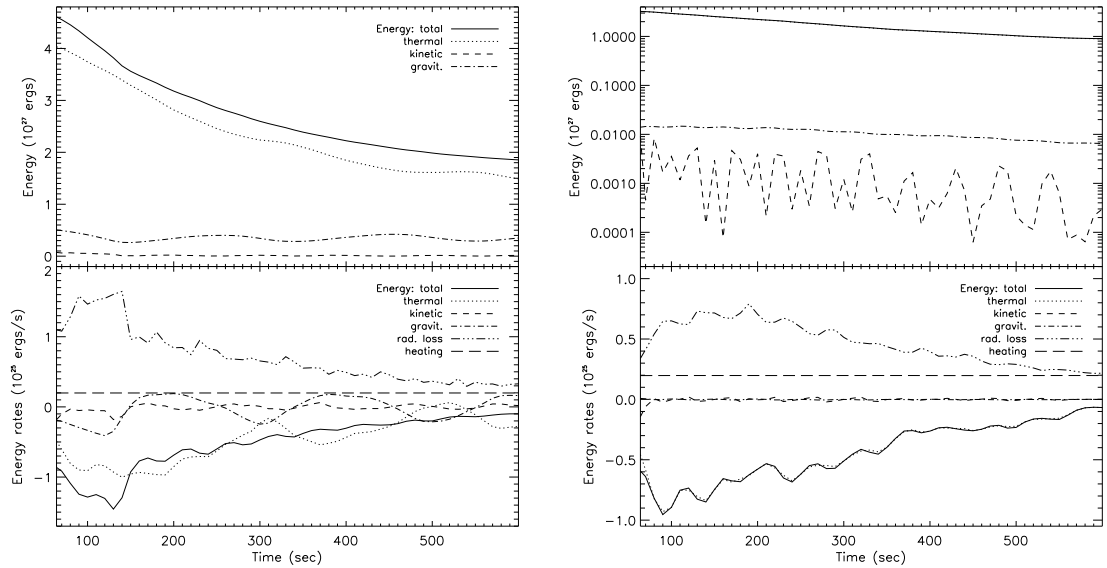

Figure 9.7: Same as Fig. 9.3, but for the whole loop (*left*) and the corona portion (*right*) of Case D, with the additional quantity, heating rate, plotted as the *long-dashed* line in the bottom panels.

Another difference here, compared with Figure 9.2 for Case A, is the short-period fluctuations in the thermal energy change rate (*dotted, bottom* panel). Such fluctuations are superimposed on the existing long-period (~ 200 s) fluctuations caused by the chromospheric oscillation. Again, we plot the energy contents in the corona and the chromosphere separately, and we find the chromosphere (not shown) has a similar energy evolution as in Case A. However, the corona behaves quite differently, as can be seen in Figure 9.7 (*right*). The above mentioned short-period fluctuations are present in the velocity (*dashed, top right*), the thermal (and total) energy change rate, as well as the radiative loss (*bottom right*). These fluctuations are caused by the traveling waves, which results in alternative compression (heating) and rarefaction (cooling) of the plasma. Such waves can also be seen in the velocity curves in Figure 9.6. The same effects are present in Case C, but not in Case B. We suggest the imposed suppression of conduction is responsible for the growth of such waves,[3] for which the strong disturbance to the fluid during the turbulent impulsive phase could be the seeds.

We also note that the lifetime of the traveling waves here may be exaggerated, because there is no viscosity included in this model. Such an approximation is good for the impulsive phase since the contribution of viscosity to the momentum and energy equations are

---

[3]Note there are similar coronal waves in Cases A and B, but they are of much smaller amplitudes and do not produce noticeable effects as in Cases C and D.

overwhelmed by the other more dramatic agents (e.g., electron heating). However, during the slow (on timescales of 10 times longer than that of the impulsive phase) evolution of the decay phase, viscosity may play a role, particularly in damping the waves.
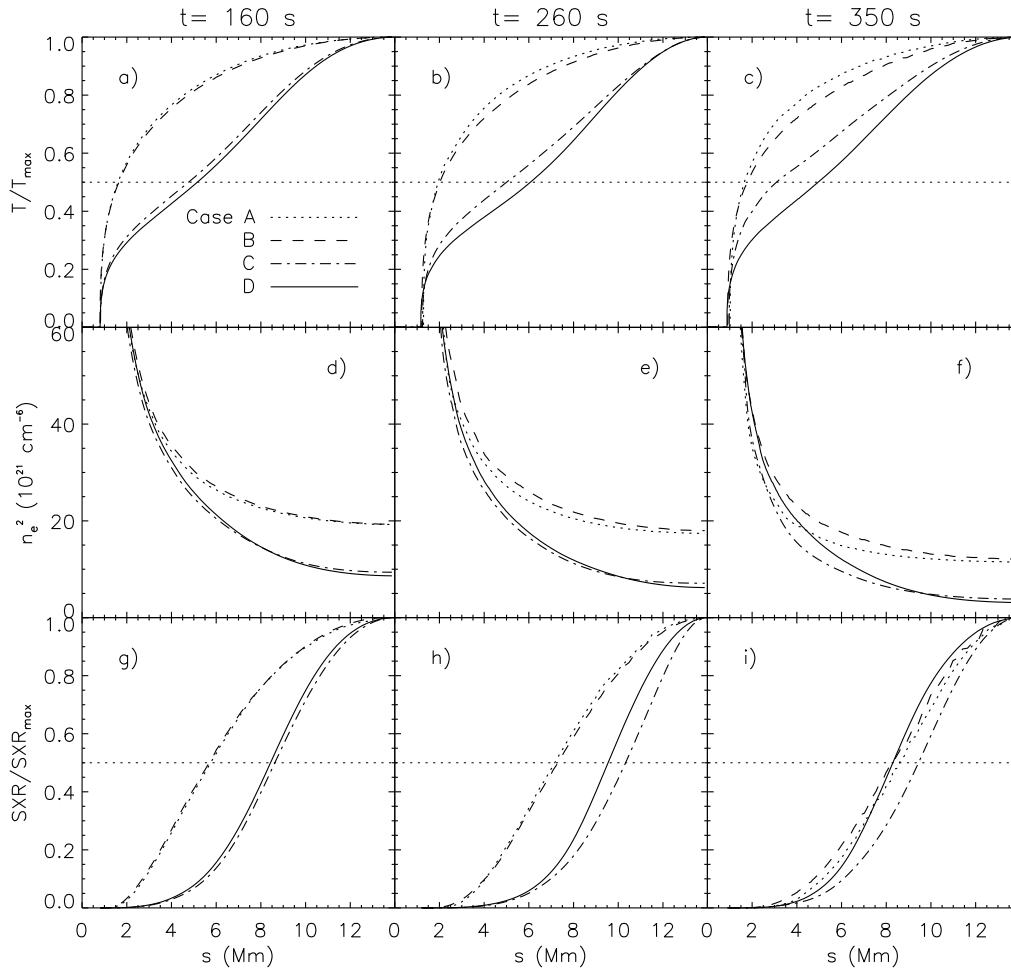
9.3.5   Comparing Cases A-D

Figure 9.8: Comparison of temperature, density squared n_e^2, and thermal bremsstrahlung emission (at 6 keV) profiles among Cases A-D at selected times. Each of the temperature and emission profiles are normalized to its individual maximum. Each column is of the same time. The dotted horizontal lines in the top and bottom rows mark the 50% levels.

We now compare the four simulation cases more directly. Figure 9.8 shows the normalized temperature (*top*) and thermal bremsstrahlung emission (*bottom*, at 6 keV) profiles, together with the density squared n_e (*middle*) at selected times for all the cases. In general, the curves of Cases A and B form one group (called Group 1), and those of Cases C and D form another (Group 2), exhibiting the expected shapes due to different conduction suppression and/or heating imposed.

Case B has a temperature profile very close to that of Case A, despite its localized heating near the LT. This is because heat conduction (without suppression) is so efficient (Jiang et al., 2006) that the energy addition by localized heating is quickly conducted away from the LT and this makes the coronal temperature close to a uniform distribution. Cases C and D have a more confined high temperature region near the LT, due to their suppressed conduction. They also have a lower coronal density because their higher coronal temperature requires less material to produce sufficient pressure.

The thermal emission profiles, in general, follow the shape of the corresponding temperature profiles. Cases C and D have narrower emission profiles, same as their temperature profiles, particularly early during the decay phase. This is consistent with that found by Jiang et al. (2006). At some other times (e.g., $t = 360$ s), this pattern does not always hold. This is because thermal emission (eq. [8.7]) is an increasing function of both T (nonlinear) and n_e^2 (or emission measure, linear). In our simulation, T increases with distance (from FP to LT), while n_e^2 behaves oppositely. The interplay of these two quantities determines the resulting thermal emission profile. It is thus not surprising that the emission profile does not necessarily follow the shape of the corresponding temperature curve exactly. Sometimes, a hump[4] (not shown) in the thermal emission can be produced and it shifts back and forth along the loop, which is due to the enhanced local density and temperature by traveling waves (see discussions above). These new features were not present in the hydrostatic solutions of Jiang et al. (2006).

Figures $9.9a$ and $9.9b$ show the history of density squared n_e^2 and temperature, respectively, at the loop apex. Again, we see that Group 1 (Cases A and B) has similar values of n_e^2, and so do Group 2 (Cases C and D) whose values are less than that of Case A by up to a factor of four. Group 1 have an increasing density at early times before its decreasing phase, while the density of Group 2 has a generally decreasing trend. This happens because in Group 1 chromospheric evaporation continues to bring material to the corona early into the decay phase, as can be seen in the large upward velocity values in Figures 9.1 and 9.4. Group 2, on the other hand, has a higher coronal temperature due to suppression and thus a higher LT pressure (see Figs. 9.5 and 9.6) that produces a downward pressure gradient force to counteracts the evaporation upflow. This results in lower upflow velocities and decreasing (and lower) LT densities in Group 2.

As to the temperature, from Case A to D, we generally have increasing values at a given time, except on the very late stage when the curves of Cases B and C cross each other. This is expected because we have increasing suppression and/or heating applied. For example, Case D combines these effects of Cases B and C together, so it has the highest LT temperature. After $t \sim 500$ s, its LT temperature even slightly increases. This comes about because of the decreasing LT density and constant continuous heating and suppression of conduction.

Figures $9.9c$ and $9.9d$ show the spatially integrated total energy and thermal XR emission flux. They also exhibit similar patterns as the LT temperature. As is evident, the n_e^2, T, and XR emission curves of Group 2 all show similar fluctuations, which are caused by the traveling waves mentioned above.

We note that the average energy decay rate (Fig. $9.9c$) of Case D (with combined

---

[4]The bright feature in X-rays moving along the loop is similar to the *TRACE* observation of the bright EUV blob that travels back and forth from one end of the loop to the other (Ryutova & Shine, 2006).
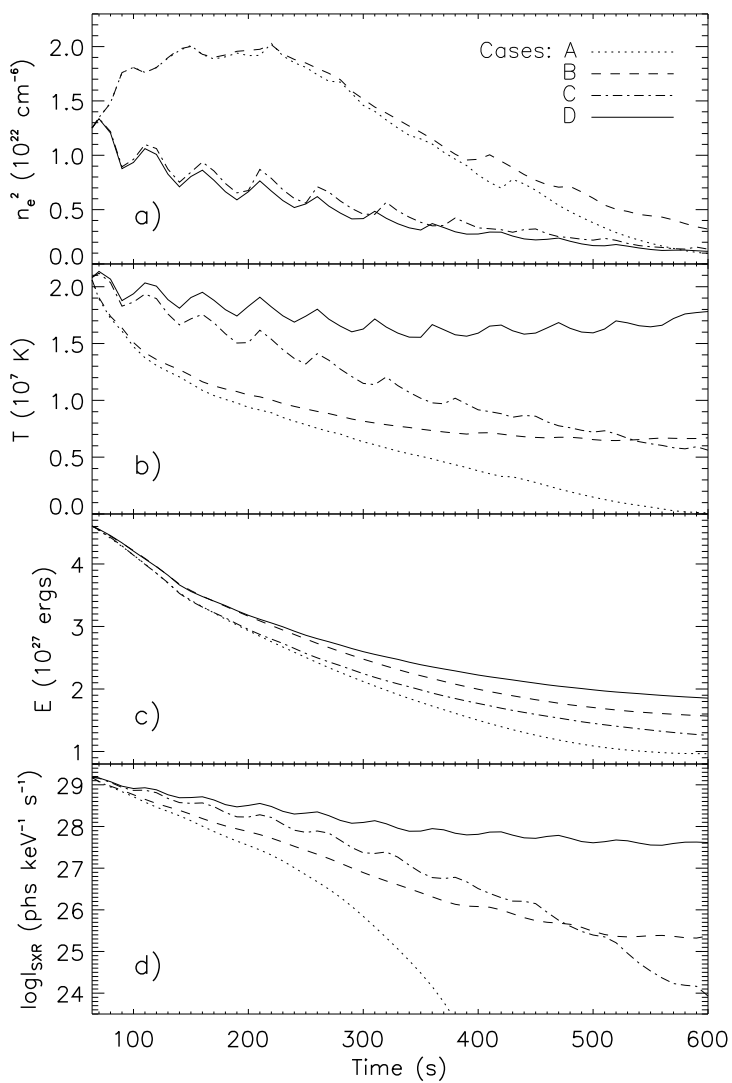
Figure 9.9: Comparison of decay of various quantities for Cases A-D. (a) and (b) Evolution of density squared n_e^2 and temperature, respectively, at the loop apex. (c) and (d) Total energy and thermal bremsstrahlung (at 6 keV) intensity I_{SXR}, respectively, both integrated over the volume of the whole loop.

suppression and heating) is about 3/4 of that of Case A. Such a difference is much less than that of Jiang et al. (2006, see Fig. 13 there), with otherwise comparable parameters. This is because they assumed hydrostatic solutions and the calculation was restricted to the hot, coronal portion of the loop, so radiative loss is small. Therefore, the only effective energy loss channel in their model is through conduction to transfer energy to the FPs. Contrastingly, here, we have plasma flow and traveling HD waves that act as another energy carrier. The energy input from the LT can be carried by plasma down to the transition region and the chromosphere and then be efficiently radiated away there.

9.4 Summary and Discussion

We have performed a HD simulation for the decay phase of solar flares, by inclusion of the fluid dynamics calculation and the chromosphere in the computational domain. This work improves on the previous work by Jiang et al. (2006) who assumed a hydrostatic condition and that by Antiochos & Sturrock (1978) who neglected radiative loss. In general, our result confirms the conclusions by Jiang et al. (2006):

1. Heating at/near the LT alone is not able to confine the LT source in a small region as seen in SXRs, although it could be invoked to explain observed energy decay rates.

2. Suppression of conduction localized near the LT is needed to produce a narrow temperature profile and thus a compact SXR source near the LT.

3. A combined heating and suppression of conduction is suggested to be present and to be localized near the LT region. Such a coexistence can explain both the reduced energy decay rates and spatially confined LT source.

 Our calculation has also uncovered some new information not present in Jiang et al. (2006):

1. Different density profiles can modify the thermal XR emission profiles based on the corresponding temperature profile. Even in the presence of a compact temperature profile, a somewhat broad XR emission profile could be produced due to the interplay of the density and temperature distributions.

2. Plasma flow and/or waves can carry energy away from the hot LT region, and thus counteract the effects of heating and suppression of conduction. Therefore, an even larger factor of suppression would be required to explain the XR observations.

 In this simple simulation study, the parameter space has not been fully explored. The width w for the Gaussian suppression profile, for example, is important in determining the effects of suppression, and in particular, the existence/growth of the traveling HD waves. The radiative loss calculation can also be improved, say, using the newly released CHIANTI package. We look forward to a future modeling development to carry out such tasks.